# Analysis on directional feature extraction for the target identification of shallow subsurface based on curvelet transform

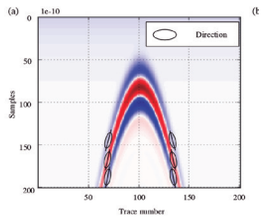


## Análisis de extracción de función direccional para la identificacion de objetos a baja profundidad en el subsuelo basado en transformada curvelet

**Yong Yang[1,2,*], Weigang Zhao[2], Yanliang Du[2] and Hao Zhang[2,3]**

[*] Corresponding author
[1] School of Mechanical, Electronic and Control Engineering, Beijing Jiaotong University, No.3 Shangyuancun, Haidian District, 100044, Beijing, China, email: sherry_0768@163.com
[2] The Key Laboratory for Health Monitoring and Control of Large Structures in Hebei Province, Shijiazhuang Tiedao University, 17 Northeast, Second Inner Ring , Shijiazhuang, 050043, Hebei, China
[3] Department of Urban & Civil Engineering, Ibaraki University, 4-12-1, Nakanarusawa 316-8511, Hitachi, Japan

**DOI: http://dx.doi.org/10.6036/8326** | Recibido: 23/10/2016 • Evaluado: 27/01/2017 • Aceptado: 03/04/2017

## RESUMEN

- La extracción de imágenes es clave para detectar e identificar objetivos someros del firme en ferrocarril por medio del georadar (GPR). Obtener imágenes apropiadas para reconocer objetivos subsuperficiales es difícil, debido a la complejidad de las estructuras sub-superficiales y la diversidad de ecos de objetivos. Para identificar esos objetivos con eficacia y eficiencia, este estudio propone un método para extracción de imagen estadístico de la energía basado en la imagen direccional del eco del objetivo. Se crearon inicialmente modelos direccionales del eco de un objetivo típico de subsuperficies someras. Se discutió la imagen direccional para diferentes ecos de objetivos. La dirección de la asíntota hiperbólica y del horizonte fueron las mayores imágenes direccionales del eco de objetivo. Se concluyó con un método de clasificación de objetivos basado en la dirección del eco. En base al análisis de la relación entre el coeficiente de Curvelet y la imagen estadística de energía en diferentes direcciones, se presentó un método de extracción de imagen para formar un vector sub-espacial de imagen. Finalmente, la clasificación y reconocimiento de objetivos se consiguió usando el método del vecino más próximo. Los resultados muestran que el método propuesto puede identificar efectivamente los problemas de huecos pre-introducidos en el firme de ferrocarriles. La precisión de la detección cumple los requisitos para la identificación de defectos en las vías de ferrocarriles. El método utilizado en este estudio no era sensible a la fase eco y era adecuado para detectar ecos de objetivos a 0º y 180º de la fase. El método propuesto facilita nuevos medios para identificar defectos en firmes de ferrocarril y es significativo para desarrollar una tecnología automática para la detección de objetivos sub-superficiales basada en GPR.
- **Palabras clave:** Radar de penetración en el suelo, georadar, Imagen direccional, Transformada de Curvelet, Método del vecino más próximo, Defectos en el firme de ferrocarriles.

## ABSTRACT

Feature extraction is the key for detecting and identifying subgrade shallow targets of railways through ground-penetrating radar (GPR). Obtaining the appropriate feature to recognize subsurface targets is difficult due to the complication of subsurface structures and the diversity of target echoes. To identify those targets effectively and efficiently, this study proposes an energy statistical feature extraction method based on the directional feature of a target echo. Directional models of a typical target echo of shallow subsurface were initially built. The directional feature of different target echoes was discussed. The direction of the hyperbolic asymptote and horizon were the major directional features in the target echo. A target classification method based on echo direction was summarized. On the basis of the analysis of the relationship between curvelet coefficient and statistical features of energy in different directions, a feature extraction method was presented to form a feature vector subspace. Finally, target classification and recognition were achieved using the nearest neighbor method. Results show that the proposed method can effectively identify the preinstalled void disease of railway subgrade. The detection accuracy met the requirements of the roadbed disease identification of railways. The method used in this study was insensitive to the echo phase, and was suitable for detecting 0° and 180° phase target echoes. The proposed method provides a new means of identifying railway subgrade diseases and is significant in developing automatic technology for subsurface target detection based on GPR.

**Keywords:** Ground-penetrating radar, Directional feature, Curvelet transform, Nearest neighbor method, Railway subgrade diseases.

## 1. INTRODUCTION

Ground-penetrating radar (GPR) is widely used in detecting the subsurface target in civil infrastructure, archaeology, and military [1-4] for its rapid, continuous, and non-destructive properties. However, GPR dataset is large, and relying on the experience of technical staff in determining subsurface targets is inefficient. For example, the operating mileage of high-speed railway in China has exceeded 20,000 km by the end of 2016; in detecting diseases inside the high-speed railway, results identified more than 100 million traces using GPR. Identifying subsurface diseases manually is challenging. Moreover, having inexperienced technical staff, fatigue and other factors will cause low efficiency, and missed and false alarm, which is unconducive for repair and maintenance work. Therefore, automatic effective detection and identification technology are the development trend of GPR.

Feature extraction is the foundation of target identification. A wide variety of targets exist in subsurface, such as pipes in civil

infrastructure, layer information in archaeology, and void diseases in reinforced concrete (RC). The features of target echoes differ in amplitude, phase and directions, because various materials possess different properties. Moreover, the crosstalk between the transmitting and receiving antennas, multiple wave, strong reflection of rebar, and background medium anisotropy clutter interference cause the GPR echo signal to show different features in time-frequency domain, which heightens the difficulty of detection. Thus, efficient extraction of target echo feature should be the focus in identifying and classifying subsurface targets.

This study focuses on the directional feature of target echoes, and proposes a new algorithm based on curvelet transform (CT) to extract target echo features and identify the target in a GPR map.

## 2. STATE OF THE ART

GPR was first used by Hülsmeyer in 1904 for the detection of metal objects [5]. Various methods have been presented by scholars to extract target features. According to different principle of data processing, those methods can be divided into two categories: image-based and echo signal-based methods.

Image-based methods regard GPR map as an image and process target echoes using digital image processing algorithm. Long and Simi [6-7] extracted the hyperbolic feature using least squares and Hough transform (HT) to detect underground mines and pipes. Wang et al. [8] improved the HT and proposed a fast HT algorithm. Freeland [9] proposed a texture feature-based method in energy, contrast, entropy, and homogeneity, and constructed the neural network classifier to categorize interlayer radar echo targets. Nath and Bhuiyan [10] used grayscale morphology for gradient extraction, contrast enhancement, and region segmentation (watershed algorithm), as well as noise removal and smoothing, which were combined with an infrared sensor to detect buried anti-personnel mines. Currently, numerous image processing algorithms can be used to process GPR maps. However, when radar signal converts to image signal, weak echo signals, such as void disease echo underneath a rebar, are easy to overlook due to the finite length of the space in each pixel, which restricts its promotion.

Echo signal-based methods extract target echo features from A- or B-scan data. Xie et al. [11] simulated void diseases in RC structure through finite-difference time-domain (FDTD) [12-13] preprocessed by predictive deconvolution and identified diseases beneath a rebar using support vector machine. Reichma et al. [14] proposed a Wiener inverse filtering method to extract features and recognize a target through singular value decomposition. Cui et al. [15] used GPR to detect sandy loam in the west of China, and presented autoregressive moving average power spectrum to estimate moisture contents and compactness values. However, given the complexity and uniqueness of the railway subgrade structure, multilayer rebar exists in ballastless track; thus, these methods cannot be applied to detect subsurface diseases.

The recent development of multiscale geometric analysis (MGA) based on wavelet provides a new idea for the extraction of directional features. Tzanis [16] proposed the CT to enhance echo signals and extract directional information. Zhang [17] used the ridgelet transform to suppress direct waves. In those cases, the MGA algorithm was always used for noise suppression but seldom used for identification and classification.

Thus, in this study, the directional features of a GPR echo signal are analyzed, and a new feature extraction method is proposed to construct a feature vector subspace and identify subsurface targets. The rest of this paper is arranged as follows. Section 3 presents a target echo directional model, and a feature space based on CT domain and utilizes nearest neighbor (NN) [18-19] method to classify targets. Section 4 discusses the process result using forward simulation and field experiment, and analyzes factors that affect feature distribution. Section 5 presents the relevant conclusions.

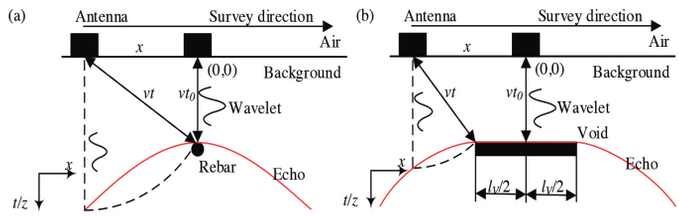


*Fig. 1: GPR echo model (a) Rebar (b) Void*

## 3. METHODOLOGY

### 3.1. TARGET ECHO DIRECTIONAL MODEL

Point target (PT, e.g., rebar) and body target (BT, e.g., cuboid) are the typical forms in subsurface structure. This section focuses on PT and BT in constructing echo models and analyzes the directional features in a GPR map.

(1) PT echo model

The PT represented by rebar and pipes is important in detecting subsurface targets using GPR. Fig. 1(a) shows the PT echo model, with rebar as an example, $x$ represents the horizontal axis; $t$ or $z$ represents the vertical axis, $t=z/v$; and $v$ is the velocity of electromagnet in the background medium. The black rectangles represent GPR antennas (transmitter/receiver antennas). The background medium parameters are $\varepsilon_r$, $\mu_r$, and $\sigma$, where $\varepsilon_r$ denotes the relative permittivity, $\mu_r$ denotes the relative permeability, and $\sigma$ denotes conductivity.

Given that the background is a low-loss medium, the velocity is constant ($v = c/\sqrt{\varepsilon_r}$, where $c$ is the speed of light). The intersection point of the vertical line passing through the rebar and air-ground interface is the coordinate origin (0, 0), and the survey direction $x$ is the horizontal coordinate, and the vertical downward direction $t/z$ is the vertical coordinate. When the antenna is at (0, 0), the two-way travel time is $t_0$; when the antenna is at ($x$, 0), the two-way travel time is $t$. In GPR, the measured data in a certain position are generally called A-scan, and the measured data along the survey direction are called B-scan. Given that function $f(x, t)$ in 2D space can be expressed as

$$f(x,t) = \frac{2}{v}\sqrt{x^2 + (vt_0/2)^2} - t \tag{1}$$

then the BT echo hyperbola can be written as a Dirac delta function, as shown as follows:

$$\delta\{f(x,t)\} = \begin{cases} 1 & f(x,t) = 0 \\ 0 & f(x,t) \neq 0 \end{cases}. \tag{2}$$

According to Maxwell equation, the electromagnetic (EM) field decays exponentially with increasing distance when the EM wave propagates in free space.

$$E = E_0 e^{-\alpha z} e^{-j\beta z} \tag{3}$$

where $E_0$ denotes the amplitude when $z$=0, and the size of amplitude associates with GPR antenna power; $\alpha$ denotes the attenuation coefficient, $\alpha=\omega[\frac{1}{2}\mu\varepsilon(\sqrt{1+(\frac{\sigma}{\omega\varepsilon})^2}-1)]^{\frac{1}{2}}$; and $\beta$ denotes the phase factor, $\beta=\omega[\frac{1}{2}\mu\varepsilon(\sqrt{1+(\frac{\sigma}{\omega\varepsilon})^2}+1)]^{\frac{1}{2}}$.

In low-loss medium, the parameters satisfy $\sigma \le \omega\varepsilon$ and $\beta \approx \omega\sqrt{\mu\varepsilon}$; thus, the phase velocity is approximately equal in all frequencies and there are only differences in amplitude between different position of target echo signals. Given that the echo attenuation function is $\gamma$, when the target location is fixed, $\gamma$ is a function of $x$ ($\gamma=\gamma(x)$), and wavelet is $w(t)$, then the GPR echo $Q(x, t)$ can be expressed as a convolution between $\delta\{f(x, t)\}$ and attenuation wavelet $\gamma(x)w(t)$ considering time $t$ is

$$Q(x,t)=\delta\{f(x,t)\}*[\gamma(x)w(t)]. \tag{4}$$

On the basis of the above analysis, the PT echo signals in GPR map show evident directional properties, which are close to the curve asymptote when $x$ tends to be infinite.

(2) BT echo model

The BT represented by void diseases is also important in subsurface structure. Fig. 1(b) shows the banded void echo model. In this case, given that the length of void is $l_V$, the intersection point of the vertical line passing through the middle point of the void and air-ground interface is the coordinate origin (0, 0), and the rest of the settings is the same as the PT echo model.

Similar with Eq. (1), given that the function $g(x, t)$ in 2D space

$$g(x,t)=\begin{cases}\frac{2}{v}\sqrt{(x+l_V/2)^2+(vt_0/2)^2}-t & x\le -l_V/2\\ t_0-t & -l_V/2<x<l_V/2\\ \frac{2}{v}\sqrt{(x-l_V/2)^2+(vt_0/2)^2}-t & x\ge l_V/2\end{cases} \tag{5}$$

then the void BT echo equation can be written as a Dirac delta function, as shown as follows:

$$\delta\{g(x,t)\}=\begin{cases}1 & g(x,t)=0\\ 0 & g(x,t)\ne 0\end{cases} \tag{6}$$

Similar with Eq. (4), GPR echoes $P(x,t)$ can be expressed as a convolution between $\delta\{g(x,t)\}$ and attenuation wavelet $\gamma(x)w(t)$ considering time $t$.

$$P(x,t)=\delta\{g(x,t)\}*[\gamma(x)w(t)] \tag{7}$$

Fig. 1(b) and Eqs. (5) and (6) prove that the echoes on the left and the right edges are the same as the part of PT echo in Fig. 1(a), and that the middle part of the echoes are horizontal.

### 3.2. DIRECTION CLASSIFICATION OF SUBSURFACE TARGET

According to Section 3.1, direction is an important feature in GPR target echo. However, the subsurface structure is complicated. For example, several diseases exist in the railway subgrade, such as frost boiling and mud pumping, as well as ballast subsidence. And sometimes all the echoes of one disease may not be displayed in a processing window; thus, on the basis of echo directional feature, subsurface targets can be divided into five categories: nontarget (NT), PT, finite BT (FBT), infinite BT (IBT), and half-infinite BT (HIBT).

(1) NT: Without a target echo, B-scan data only contain noise signal. For example, GPR echo signals are only composed of medium anisotropy echo, which is caused by the uneven mixing of concrete aggregates.

(2) PT: When the target vertical cross-sectional area is very small, the distance between the antenna and every point on the target can be regarded as a fixed value. Then, the target is called PT. For example, the diameter of a rebar in a ballastless track is considerably small. The diameter of the upper pre-stressing tendon is $\Phi$=10 mm in CRTS-II slab ballastless track. A hyperbolic feature of the echo is relatively clear, and the horizontal part is limited. Here, the rebar can be called a PT.

(3) FBT: When the horizontal part of the target echo is relatively long, but all the echoes can still be included in a processing window (Fig. 1(b)). These targets include void diseases of concrete-asphalt (CA) mortar in a ballastless track structure, frost boiling, and mud pumping diseases in a ballast track structure.

(4) IBT: When the length of the target is sufficiently large, only the horizontal part of the echoes exists in a processing window, such as the interface echo of the subgrade top and bottom layers.

(5) HIBT: When the length of the target is between FBT and IBT, the parts of the edge and horizontal echoes exist in a processing window. According to the different side echo signals detected by GPR, HIBT can be divided into HIBT left (HIBTL) and HIBT right (HIBTR). The left represents entrance direction, and the right represents departure direction.

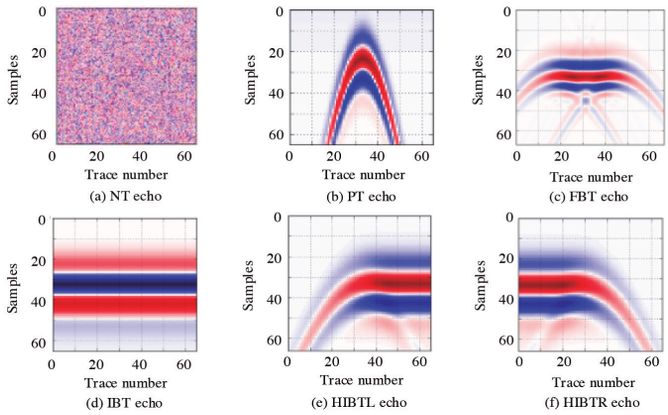

*Fig. 2: Different target echoes in B-scan*

As shown in Fig. 2, different types of target echo exist in different directions. Fig. 2(a) for NT echo is composed of a noise signal without a directional feature. Fig. 2(b) for PT echo shows a hyperbolic feature, which is consistent with the direction of the asymptote. Symmetry distribution exists in the position of a PT. Fig. 2(c) for FBT echo shows a part of the hyperbolic feature at the edge with the directions of the asymptote and the horizon in the middle part. The length of the horizontal part concerns with the length $l_V$ of the target. When $l_v \to 0$, the type of the target changes from FBT to PT; when $l_v \to \infty$, the type of the target changes from FBT to IBT. Fig. 2(d) for IBT echo shows a horizontal direction, which is the same as the middle part of the FBT echo. Fig. 2(e) for HIBTL shows the left part of the hyperbolic feature with the direction of the asymptote and the horizontal part with the direction of the horizon. Fig. 2(f) for HIBTR shows the right part of the hyperbolic feature with the direction of the asymptote and the horizontal part with the direction of the horizon.

### 3.3. DISCRET CT (DCT)

CT is an MGA method proposed by Candès and Donoho et al. [20-23]. This method overcomes the limitation of the wavelet

transform in 2D image singular analysis. The development process of CT has experienced ridgelet transform [20], particularly the first and second generations of CT [21-23]. The current study focuses on the second-generation CT.

According to Radon transform (RT) [24-25] and projection slice theorem [26], the RT and 2D Fourier transform (2D-FT) can be written as

$$Rf(\theta,t)=\int_{R^2} f(x_1,x_2)\delta(x_1\cos\theta+x_2\sin\theta-t)dx_1dx_2 \quad (8)$$

$$F(u,v)=\int_{-\infty}^{\infty} R_f(\theta,t)\exp(-j2\pi qp)dp \quad (9)$$

where $Rf(\theta, t)$ denotes the RT of $f(x_1, x_2)$, which indicates the line integral of the function $f(x_1, x_2)$ with direction θ and intercept $t$. $F(u, v)$ denotes 2D-FT. The relationship between RT and 2D-FT can prove that the 1D inverse FT (IFT) in direction θ is the RT. Thus, the projection in a certain direction in the 2D-FT space also reflects the feature of the corresponding direction in the 2D space-time domain. On this basis, the ridgelet transform and the first-generation CT are proposed according to the multiscale wavelet transform of the line integral in a certain direction.

In 2002, Candès and Donoho [21] proposed the second-generation CT based on radial window $W_j$ and angular window $V_l$.

$$c(j,l,k)=\left\langle f,\varphi_{j,l,k}\right\rangle=\int_{R^2} f(x_1,x_2)\varphi^*_{j,l,k}(x_1,x_2)dx \quad (10)$$

where $c(j, l, k)$ denotes the curvelet coefficient; $j$, $l$, and $k$ denote scale, direction, and translation, respectively, $k=(x_1, x_2)$; $\varphi_{j,l,k}$ denotes the "mother" curvelet; and the superscript "*" denotes the conjugate.

In 2005, Candès and Donoho et al. [22] utilized the Cartesian coordinate to replace the polar coordinate, built the discrete CT (DCT), and proposed two digital implementations: unequally spaced fast Fourier transforms and swapping. DCT is shown as follow:

$$c^D(j,l,k)=\sum_{0\le x_1,x_2<n} f(x_1,x_2)\varphi^{D*}_{j,l,k}(x_1,x_2) \quad (11)$$

where $c^D(j,l,k)$ denotes discrete curvelet coefficient, $\varphi^D_{j,l,k}$ is the discrete "mother" curvelet, and the superscript $D$ denotes digital.

Fig. 3 (see section: supplementary material) presents the time-frequency feature of CT. In Fig. 3(a), a multiscale decomposition is shown in a Cartesian coordinate in frequency domain. In this figure, the data matrix size is (256, 256), and according to CT, the data can be divided into five layers: coarse layer, Scales 2-4, and the finest layer. The coarse and the finest layers represent low and high frequencies, respectively, and Scales 2-4 represent detail layers in middle-high frequencies. The directional resolutions of the coarse and finest layers are both one, those of Scales 2-4 are 16, 32, and 32, respectively. The colored part in Fig. 3(a) denotes the middle- and high-frequency bandpass filters, where $\theta=\pi/4$ ($l=8$) in Scale 3. Fig. 3(b) presents a detailed 3D graphics of the colored part of Fig. 3(a). Fig. 3(c) shows the directional resolutions of the coarse layer, and Scales 2 and 3.

### 3.4. FEATURE EXTRACTION OF GPR TARGET ECHO

In Sections 3.1 and 3.3, the directional feature of GPR target echo and the sensitive direction of CT have been studied. According to Eq. (13), $c^D(j,l,k)$ represents coefficient in scale $j$, direction $l$, and translation $k$, and mother curvelet $\varphi^D_{j,l,k}(x_1, x_2)$ is orthogonal. Thus, based on frame theory and Parseval theorem, the 2D GPR map of the B-scan $f(x_1, x_2)$ can be written as follows:

$$f(x_1,x_2)=\left\langle c^D(j,l,k),\varphi^D_{j,l,k}(x_1,x_2)\right\rangle \quad (12)$$

Therefore, the sum of $c^D(j,l,k)$ in different translation positions $K(k_1, k_2)$denotes energy statistical feature in scale $j$ and direction $l$.

$$s_{j,l}=\sum_{k1}\sum_{k2}|c^D(j,l,k)| \quad (13)$$

where $s_{j,l}$ represents the energy statistical feature in $j$ and $l$.

The five types of target echo are processed by CT, and the energy statistical feature is shown as follows.

(1) NT echo feature

In NT echo, the GPR map is only composed of medium anisotropy echo, which is caused by the uneven mixing of concrete aggregates. Generally, the medium parameters of uneven mixing follow the Gaussian distribution [27]. The 2-dB white Gaussian noise is used to replace the NT echo with echo data matrix size (200, 200). Then, the CT turns the matrix into five layers in the frequency domain, namely, coarse layer, Scale 2-4, and the finest layer. In the coarse and finest layers, the directional resolutions are both one, which implies that the IFT result represents all the directions within [−π, π]; thus these parts are ignored in this study. Fig. 4 (see section: supplementary material) shows the curvelet coefficient summary in different scales and directions, and the statistical distributions of energy in different scales and directions still follow random distribution. The directional resolutions of Scales 2-4 are 16, 32, and 32, respectively. Interpolation is performed on Scale 2 to compare the energy distribution of different scales and directions in one figure.

(2) PT echo feature

In PT echo, given that background medium parameters are ($\varepsilon_r$, $\mu_r$, σ)=(6,1,0.1), and rebar is PT. FDTD and finite element methods [28] are often used for data simulation. In this study, software gprMax [29-30] based on FDTD is used for forward simulation with echo data matrix size (200, 200). Then, the echo data are processed by CT, and the statistical feature of the energy is obtained in different scales and directions. Fig. 5(a) shows the simulation result, where the long axis of the ellipse represents the direction. Energy is mainly concentrated in the direction of the hyperbolic asymptote.

Fig. 5(b) shows the statistical feature of the energy on Scales 2-4, where the energy is mainly concentrated in directions $l=\{11,12,13,14,27,28,29,30\}$. The angle θ corresponding to the directions is $\theta\in[-5\pi/8,-3\pi/8]\cup[3\pi/8,5\pi/8]$.

(3) IBT echo feature

The feature of IBT echo is similar with that of PT echo, except that a different medium layer is regarded as IBT.

Fig. 5(c) shows the simulation result with echo data matrix size (200, 200). Fig. 5(d) shows the statistical feature of the energy in Scales 2-4, where the energy is mainly concentrated in directions $l=\{4,5,20,21\}$. The angle θ corresponding to the directions is $\theta\in[-\pi/8,\pi/8]\cup[7\pi/8,9\pi/8]$.

(4) Other types of target echo feature

According to the above analysis, PT and IBT echoes possess directional features in the statistical distribution of energy based on CT; the distribution maintains consistency with different scales. However, in Fig. 5(b), more information is represented on Scale 3, with the energy attenuation in directions $l=\{12,13,28,29\}$. Thus,

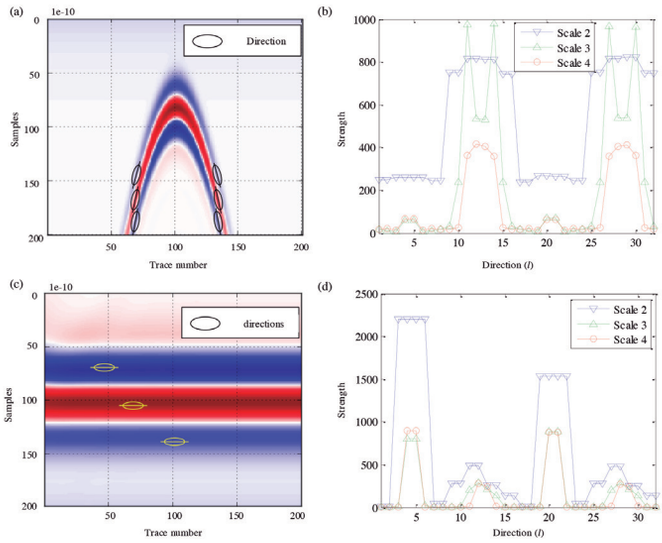


*Fig. 5: Echoes and statistical features of energy:(a) PT echo simulation result; (b) Statistical feature of the CT energy of PT echo; (c) Simulation result of IBT echo; (d) Statistical feature of the energy of IBT echo*

for FBT and HIBT, only the statistical feature of energy on Scale 3 is considered. As shown in Fig. 6, normalization is performed to analyze the direction in the same proportion.

$$s'_{j,l} = \frac{s_{j,l}}{\sum_{l} s_{j,l}} \tag{14}$$

The FBT echo energy is mainly concentrated in directions $l$={4,5,20,11,12,13,14,27,28,29,30}. The angle θ corresponding to the directions is $\theta \in [-\frac{\pi}{8},\frac{\pi}{8}]U[7\frac{\pi}{8},9\frac{\pi}{8}]U[-5\frac{\pi}{8},-3\frac{\pi}{8}]U[3\frac{\pi}{8},5\frac{\pi}{8}]$. Similar with the Scale 3 on Fig. 5(b), the energy attenuates in directions $l$={12,13,28,29}, where directions $l$={4,5,20,21} and $l$={11,12,13,14,27,28,29,30} represent the energy of the horizontal and edge parts, respectively.

The energies of the HIBTL and HIBTR echoes are mainly concentrated in directions $l$={11,12,13,14,27,28,29,30}. The distribution is essentially consistent with the PT echo but is not symmetric in $\theta=\pm\frac{\pi}{2}$. By contrast, the energy distributions of HIBL and HIBR are symmetric in $\theta=\pm\frac{\pi}{2}$.

The energy contribution of different targets in circumferential phase [–π, π] is shown in Fig. 7 (see section: supplementary material).

### 3.5. TARGET CLASSIFICATION

The statistical features of the energy of different targets gained by the CT on Scale 3 form a 32-dimension vector subspace, and the feature in each target is a point in the subspace

$$S_i = (s'_{i,1}, s'_{i,2}, \ldots, s'_{i,l}, \ldots, s'_{i,32})^T \tag{15}$$

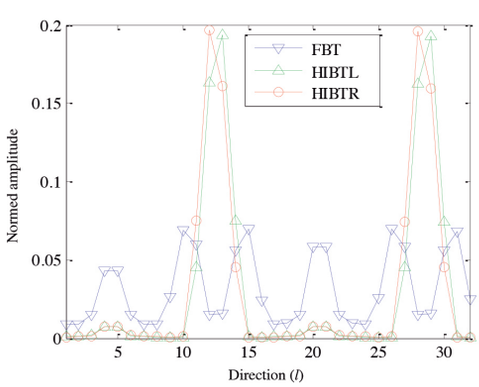


*Fig. 6: Comparison between different targets on Scale 3*

where superscript $T$ represents vector transpose, $j$=3, $l$=1,2⋯, 32, $i$=1,2⋯, 6, and $i$ represents NT, PT, IBT, FBT, HIBTL, and HIBTR, respectively. Matrix $S=\{S_1, S_2, \cdots, S_6\}$ consists of feature subspace. For NT, directional feature does not exist on all scales; thus, $S_1=(0,0,\cdots,0)$, which is the origin point in the 32-dimension subspace.

A partition of the six-feature vector in a subspace based on NN is shown in Fig. 8 (see section: supplementary material).

Given that the unknown GPR echo sample is $C$, the feature vector of $C$ on Scale 3 is $S_x$. Then, the distance between $S_x$ and $S_i$ can be expressed as follows:

$$d_i = \| S_i - S_x \| \tag{16}$$

According to NN, sample $C$ belongs to classification $i$, where

$$i := \arg\min_i d_i \tag{17}$$

The algorithm flow based on directional feature extraction and recognition is shown as follows:

(1) The relative permittivity of background medium $\varepsilon_r$ is determined;
(2) According to $\varepsilon_r$, models based on the six types of target are constructed, and forward simulations are executed;
(3) Feature vectors $S_i$ on Scale 3 are formed using CT, and subspace $\{S_i\}$, $i$=1⋯ 6 is built;
(4) GPR echo sample $C$ is obtained on the basis of detection;
(5) Preprocessing is performed to depress the direct wave etc., and echo $C$ changes to $C_1$;
(6) CT is processed on $C_1$, and feature vector $S_x$ is achieved;
(7) NN algorithm is executed to realize the classification according to Eqs. (16)and (17).

## 4. RESULT ANALYISIS AND DISCUSSION

### 4.1. EXPERIMENT

To verify the proposed algorithm, void diseases in RC structure were concerned in this study, and a field experiment was conducted at the No. 2 Project of the Engineer Training Center in Shijiazhuang Tiedao University. The preinstalled void disease is composed of polystyrene foam with 20 cm length, an RIS-K2 system constructed by IDS (Ingegneria dei Sistemi SpA, Italy) is used with 900 MHz antenna. The disease arrangement, detection, and processing result are shown in Fig. 9 (see section: supplementary material).

Fig. 9 (d) reveals the statistical feature of the energy on Scale 3; the NN classification method is processed. Result is shown in Fig. 10 that the shortest distance exists between the feature vector of sample echo and that of the simulated FBT echo with $d$=0.067, which is consistent with the preinstalled diseases.

### 4.2. INFLUENCE OF RELATIVE PERMITTIVITY ON THE FEATURE

For PT, FBT, and HIBT, the direction of the asymptote is important in distinguishing them from the IBT. The wave velocity $v$ is directly affected by the relative permittivity of the background medium; the directional feature of the target echo is related to wave velocity $v$.

According to Eqs. (1) and (2), the asymptote of a hyperbola can be written as follows:

$$\frac{dt}{dx} = \pm 2\sqrt{\varepsilon_r}/c \tag{18}$$

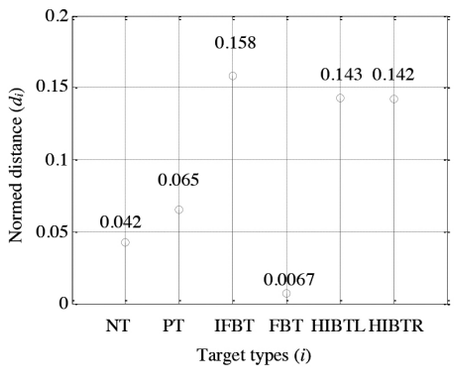


*Fig. 10: Distances between the sample echo and the simulated echoes*

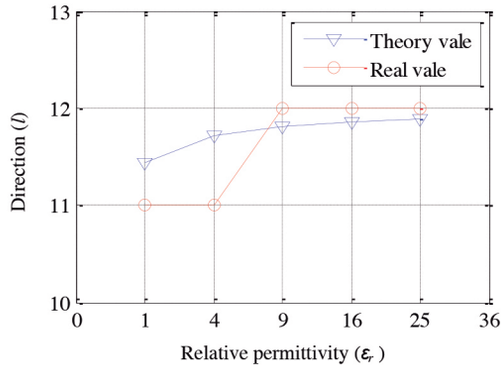


*Fig. 11: Energy distribution between different permittivities*

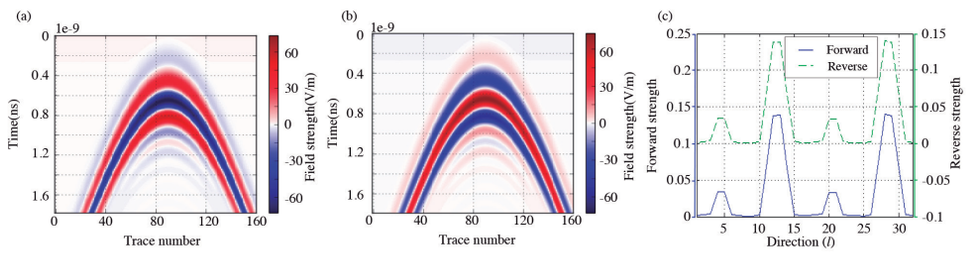


*Fig. 12: Features comparison between the forward and reverse simulations on Scale 3: (a) Forward direction simulation; (b) Reverse direction simulation; (c) Processing results on Scale 3*

The discretization of time and survey direction is needed in mesh division. Given that trace interval between A-scans is $\Delta x$, and the time interval between the samples in an A-scan is$\Delta t$, the discretized asymptote can be expressed as follows:

$$\frac{dm}{dn} = \pm \frac{2\sqrt{\varepsilon_r}\Delta x}{c\Delta t} \tag{19}$$

where $n$ and $m$ denote the horizontal and vertical grids, respectively; $x=n\Delta x$; and $t=m\Delta x$.

For example, given that sample window $t$=6 ns, sample points are 1000 points, $\Delta t=6x10^{-12}$ *ns*, and trace interval $\Delta x=2$ *mm*. On Scale 3, directional resolution is $2\pi/32$, and an interval $[-\pi/2, 0]$ is divided into 8 parts equally, representing directions $l$ from 5 to 12, respectively. Generally, the relative permittivity $\varepsilon_r$ of the background medium lies in interval [1, 25]. Thus, given that $\varepsilon_r = \{1,4,9,16,25\}$ forward simulations are processed. The energy distribution is shown in Fig. 11. The blue and red lines represent the theory distribution and simulated results, respectively. When relative permittivity $\varepsilon_r$ changes, the energy feature of the hyperbola asymptote is mainly distributed in the interval $[-7\pi/16, -\pi/2]$ ($l=\{11,12\}$)). However, distribution changes occur on $\varepsilon_r \in [4,9]$. Therefore, velocity estimation or relative permittivity detection should be implemented before the construction of the feature subspace.

### 4.3. INFLUENCE OF TARGET ECHO PHASE ON THE FEATURE

Different echo phases may occur in various surfaces. According to the law of reflection regarding EM wave, reflection coefficient $r_i$ can be expressed as

$$r_i = \frac{\eta_{i+1} - \eta_i}{\eta_{i+1} + \eta_i} \tag{20}$$

where $n_i$ denotes the wave impedance of the $i$th layer medium. When $\eta_{i+1}-\eta_i>0$, $r_i$ is positive, and the echo phase of the reflection wave is the same to that of the incident wave (0° phase). By contrast, when $\eta_{i+1}-\eta_i<0$, $r_i$, is negative, and the echo phase of the reflection wave is opposite to that of the incident wave (180° phase). For example, given that the background medium of PT is $\varepsilon_r$=1, the target medium is $\varepsilon_r$=9, and forward simulations are processed. The forward and reverse results are shown in Figs. 12(a) and 12(b). Fig. 12(c) shows the processing result of the statistical features of the energy. The two curves reveal that the energy feature is exactly the same in every direction. Thus, the proposed algorithm is insensitive to echo phase, and is applicable to 0° and 180° phases.

### 4.4 INFLUENCE OF VOID SIZE ON CLASSIFICATION

The length $l_V$ of void plays an important role in classification based on direction. When the length $l_V$ approaches zero, the void target is regarded as a PT; when the length $l_V$ approaches infinity, the void target is regarded as an IBT; and when the length $l_V$ is between zero and infinite, the void target is regarded as an FBT or HIBT. Thus, void size affects classification. Simulations are conducted to analyze the accuracy of classification.

Given that background medium parameters are ($\varepsilon_r$, $\mu_r$, $\sigma$)=(6,1,0.1), the grid size is 2 mm × 4 mm. Moreover, given that void length for PT is 1 cm and that for FBT is 20 cm, then simulations are performed when the length $l_V$ is equal to {1, 2, 3, 4, 5, 6, 7, 8, 15, 20}. Classification results are shown in Table 1, when the void length is less than or equal to 4 cm, the voids are classified as PT, and others are classified as FBT.

In detecting railway roadbed diseases with ballastless track, when the length of void disease is less than 8 cm in CA mortar, the stress of the track structure is not more than its strength, and the track structure is considered safe. Thus, the proposed algorithm satisfies the requirements of identifying railway roadbed diseases.

## 5. CONCLUSION

To overcome the difficulty of target recognition caused by the complexity of target echo, a feature extraction and target identification method based on the directional feature of a target echo were proposed in this study. The principal directional features of target echoes were initially analyzed. Then, feature extraction of shallow subsurface targets and identification method were performed based on the directional selectivity of CT. The following conclusions are drawn:

(1) The direction of the target echo is an important feature of GPR. For PT echo, the direction of the hyperbolic asymptote

| Void length $l_v$ (cm) | NT | PT | FBT | IBT | HBTL | HBTR | Result |
|---|---|---|---|---|---|---|---|
| 1 | 0.231 | 0 | 0.023 | 0.537 | 0.131 | 0.145 | PT |
| 2 | 0.239 | 0.013 | 0.029 | 0.546 | 0.134 | 0.149 | PT |
| 3 | 0.243 | 0.023 | 0.035 | 0.550 | 0.141 | 0.157 | PT |
| 4 | 0.237 | 0.024 | 0.027 | 0.546 | 0.150 | 0.164 | PT |
| 5 | 0.231 | 0.025 | 0.020 | 0.539 | 0.152 | 0.167 | FBT |
| 6 | 0.221 | 0.040 | 0.023 | 0.531 | 0.163 | 0.178 | FBT |
| 7 | 0.204 | 0.070 | 0.050 | 0.517 | 0.177 | 0.190 | FBT |
| 8 | 0.215 | 0.045 | 0.027 | 0.522 | 0.149 | 0.161 | FBT |
| 15 | 0.228 | 0.019 | 0.011 | 0.536 | 0.142 | 0.156 | FBT |
| 20 | 0.224 | 0.023 | 0 | 0.535 | 0.146 | 0.159 | FBT |

*Table 1: Influence of void size on identification*

is the principal directional feature. For IBT echo, the direction of the horizon is the principal directional feature. For FBT and HIBT, the directional features are the linear combination of PT and IBT.

(2) The statistical feature of the energy on the Scale 3 of CT represents the energy distribution of different targets in various directions. Calculation results show that the energy in the horizon distributes in directions $l$={4,5,20,21}. The energy in the asymptote is related to relative permittivity and is symmetric with directions $l$={12,13}/{28,29}.

(3) The 32-dimension feature subspace based on the statistical feature of energy and the NN method are effective and efficient in classifying subsurface targets. The forward simulation and field experiment show that the proposed method is insensitive to the echo phase and satisfies the requirements of identifying railway subgrade diseases.

The classification method used in this study overcomes the problems of low efficiency and high missed/false alarm rate by manual. It is significant to generalize GPR to detect the diseases in railway subgrade, which has the properties of long distance and large data. However, the objects in this study are point and banded sharps along the survey line. The applicability of the proposed method to singular sharps, for example ball and funnel, needs further discussion. Meanwhile, the large amount of disease detection data in railway roadbed leads to the requirement of the sparse representation , such as the types, shapes, and locations of diseases. Thus, this study is only a part of disease sparse representation, and the rest of the research should be further explored.

## BIBLIOGRAPHY

[1] Grandjean G, Gourry J C, Bitri A. "Evaluation of GPR techniques for civil-engineering applications: study on a test site". Journal of Applied Geophysics. October 2000. Vol. 45-3. p.141-156. DOI: http://dx.doi.org/10.1016/S0926-9851(00)00021-5
[2] Malagodi S, Orlando L, Piro S, et al. "Location of Archaeological Structures using GPR Method: Three-dimensional Data Acquisition and Radar Signal Processing". Archaeological Prospection. March 1996. Vol. 3-1. p.13-23. DOI: http://dx.doi.org/10.1002/(SICI)1099-0763(199603)3:1<13::AID-ARP37>3.0.CO;2-4
[3] Kositsky J, Amazeen C A. "Results from a forward-looking GPR mine detection system". Proceedings of SPIE - The International Society for Optical Engineering. March,2001. p.700-711. DOI: http://dx.doi.org/10.1117/12.445523
[4] Khakiev Z, Shapovalov V, Kruglikov A, et al. "GPR determination of physical parameters of railway structural layers". Journal of Applied Geophysics. July,2014. Vol. 106-7. p.139-145. DOI: http://dx.doi.org/10.1016/j.jappgeo.2014.04.017
[5] Gaspare G. 100 Years of Radar. Springer International Publishing, 2016. 399 p. ISBN: 978-3-319-00584-3
[6] Long K, Davidson N. "Image processing of ground penetrating radar data for landmine detection". Proceedings of SPIE - The International Society for Optical Engineering. May 2006. Vol. 6217. p.1-12. DOI: http://dx.doi.org/10.1117/12.664038
[7] Simi A, Bracciali S, Manacorda G. "Hough transform based automatic pipe detection for array GPR: Algorithm development and on-site tests". Radar Conference. May, 2008. p.1-6. DOI: http://dx.doi.org/10.1109/RADAR.2008.4720763
[8] Wang J, Su Y. "Fast Detection of GPR Objects with Cross Correlation and Hough Transform". Progress in Electromagnetics Research C. August, 2013. Vol. 38. p.229-239. DOI: http://dx.doi.org/10.2528/PIERC13022510
[9] Freeland R S. "Subsurface Characterization using Textural Features Extracted from GPR Data". Transactions of the Asabe. January 2007. Vol. 50-1. p.287-293.DOI: http://dx.doi.org/10.13031/2013.22392
[10] Nath B, Bhuiyan A. "A Geometrical Feature Based Sensor Fusion Model of GPR and IR for the Detection and Classification of Anti-Personnel Mines" International Conference on Intelligent Systems Design and Applications. IEEE. November 2007. p.849-856. DOI: http://dx.doi.org/10.1109/ISDA.2007.21
[11] Xie X, Qin H, Yu C, et al. "An automatic recognition algorithm for GPR images of RC structure voids". Journal of Applied Geophysics. Decemeber 2013. Vol. 99-12. p.125–134. DOI: http://dx.doi.org/10.1016/j.jappgeo.2013.02.016
[12] Ando Y. "Implementation of the Perfect Matched Layer to the CIP Method". Ieice Transactions on Electronics. May 2006. Vol. 89-5. p.645-648. DOI: http://dx.doi.org/10.1093/ietele/e89-c.5.645
[13] Solla M, Asorey-Cacheda R, Núñez-Nieto X, et al. "Evaluation of historical bridges through recreation of GPR models with the FDTD algorithm". Ndt & E International. January 2016. Vol. 77. p.19-27.DOI: http://dx.doi.org/10.1016/j.ndteint.2015.09.003
[14] Reichman D, Morton K D, Collins L M, et al. "Target localization and signature extraction in GPR data using expectation-maximization and principal component analysis". Proceedings of SPIE - The International Society for Optical Engineering. May, 2014. Vol. 9072-3. p.1-19. doi: http://dx.doi.org/10.1117/12.2049874
[15] Cui F, Wu Z Y, Wang L, et al. "Application of the Ground Penetrating Radar ARMA power spectrum estimation method to detect moisture content and compactness values in sandy loam". Journal of Applied Geophysics. September 2015. Vol. 120. p.26-35. DOI: http://dx.doi.org/10.1016/j.jappgeo.2015.06.006
[16] Tzanis A. "The Curvelet Transform in the analysis of 2-D GPR data: Signal enhancement and extraction of orientation-and-scale-dependent information". Journal of Applied Geophysics. February, 2015. Vol. 115-2C. p.145-170. DOI: http://dx.doi.org/10.1016/j.jappgeo.2015.02.015
[17] Zhang Z Y, Zhang J L, Yu H Y, et al. "Ridgelet transform with application in ground penetrating radar processing". International Conference on Wavelet Analysis and Pattern Recognition. IEEE Xplore. January 2007. p. 1054-1059.DOI: http://dx.doi.org/10.1109/ICWAPR.2007.4421588
[18] Dhurandhar A, Dobra A. "Probabilistic characterization of nearest neighbor classifier". International Journal of Machine Learning and Cybernetics. April 2013. Vol. 4-4. p.259-272. DOI: http://dx.doi.org/10.1007/s13042-012-0091-y
[19] Belongie S, Malik J, Puzicha J. "Shape matching and object recognition using shape contexts". IEEE Transactions on Pattern Analysis & Machine Intelligence. August 2010. Vol. 24-4. p.509-522. DOI: 10.1109/34.993558
[20] Candès E J. "Ridgelets and the Representation of Mutilated Sobolev Functions". Siam Journal on Mathematical Analysis. March 2000. Vol. 33-2. p.347-368. DOI: 10.1137/S003614109936364X
[21] Candès E J, Donoho D L. "New tight frames of curvelets and optimal representations of objects with piecewise C2 singularities". Communications on Pure and Applied Mathematics. November 2004. Vol. 57-2. p.219-266. DOI: 10.1002/cpa.10116
[22] Candès E J, Demanet L. "The curvelet representation of wave propagators is optimally sparse". Communications on Pure and Applied Mathematics. March 2005. Vol. 58-11. p.1472–1528. DOI: http://dx.doi.org/10.1002/cpa.20078
[23] Candès E J, Demanet L, Donoho D L, et al. "Fast Discrete Curvelet Transforms". Multiscale Modeling & Simulation. September 2006. Vol. 5-3. p.861-899. DOI: http://dx.doi.org/10.1137/05064182X
[24] Karabchevsky A, Karabchevsky S, Abdulhalim I. "Fast surface plasmon resonance imaging sensor using Radon transform". Sensors & Actuators B Chemical. July 2011. Vol. 155-1. p.361-365. DOI: http://dx.doi.org/10.1016/j.snb.2010.12.012
[25] Matus F, Flusser J. "Image representation via a finite Radon transform". IEEE Transactions on Pattern Analysis & Machine Intelligence. August 1993. Vol. 15-10. p.996-1006.DOI: http://dx.doi.org/10.1109/34.254058
[26] Ng R. "Fourier slice photograph". Acm Transactions on Graphics. July 2005. Vol. 24-3. p.735-744.DOI: http://dx.doi.org/10.1145/1186822.1073256
[27] Jiang Z, Zeng Z, Li J, et al. "Simulation and analysis of GPR signal based on stochastic media model with an ellipsoidal autocorrelation function". Journal of Applied Geophysics, March 2013, Vol. 99-3. p.91-97. DOI: http://dx.doi.org/10.1016/j.jappgeo.2013.08.005
[28] Wang Y, Lu Y J, Si C D. "Tire-Pavement Coupling Dynamic Simulation under Tire High-Speed-Rolling Condition". International Journal of Simulation Modelling. June, 2016. Vol. 15-2. p.236-248. DOI: http://dx.doi.org/10.2507/IJSIMM15(2)4.332
[29] Warren C, Giannopoulos A, Giannakis I. "An advanced GPR modelling framework: The next generation of gprMax". International Workshop on Advanced Ground Penetrating Radar. October 2015. p.1-4.DOI: http://dx.doi.org/10.1109/IWAGPR.2015.7292621
[30] Giannakis I, Giannopoulos A, Warren, C. "A Realistic FDTD Numerical Modeling Framework of Ground Penetrating Radar for Landmine Detection" IEEE Journal of Selected Topics in Applied Earth Observations and Remote Sensing. August 2016. Vol. 9-1, p.37-51. DOI: http://dx.doi.org/10.1109/JSTARS.2015.2468597

## APPRECIATION

This study was financially supported by National Natural Science Foundation of China (No. 51578349) and the Railway Ministry of Science and Technology Research and Development Program of China (No. 2013G004-A-1).

## SUPPLEMENTARY MATERIAL

http://www.revistadyna.com/documentos/pdfs/_adic/8326-1.pdf